2018

Advanced Air-Side Heat Transfer Surface Geometries Enabled by Additive Manufacturing

Courtney Leeds
University of Madison-Wisconsin, United States of America, cleeds@wisc.edu

Cassandra Wright
University of Madison-Wisconsin, United States of America, cwright25@wisc.edu

Gregory F. Nellis
University of Wisconsin, United States of America, gfnellis@engr.wisc.edu

Advanced Air-Side Heat Transfer Surface Geometries Enabled by Additive Manufacturing

Courtney LEEDS[1]*, Cassandra WRIGHT[2], Gregory NELLIS[3]

[1,2,3]University of Wisconsin-Madison,
Department of Mechanical Engineering,
Madison, WI 53706 USA
Email: [1]cleeds@wisc.edu, [2]cwright25@wisc.edu,
[3]gfnellis@engr.wisc.edu

* Corresponding Author

ABSTRACT

To maintain the performance of power plants while switching from water-cooling to air- (or dry-) cooling it is necessary to develop low-cost high-performance heat exchangers. Additive manufacturing using highly-filled polymers that provide increased conductivity and design freedom for manufacturing provide one path towards this goal. Advanced air-side heat transfer surface geometries enabled by additive manufacturing are being explored. One option is the axially-tapered (i.e., hourglass-shaped) pin fin array geometries considered in this work using Computational Fluid Dynamics (CFD). The axially-tapered pin fin uses less material than a conventional, provides higher heat transfer coefficient for most configurations (due to the small, on average, diameter) (Žukauskas, 1972), and provides a larger open area for air flow and thus a lower pressure drop. The fins can be manufactured such that they are hollow, allowing water flow into them and thus reducing the conduction resistance further. This paper uses ANSYS Workbench (ANSYS, 2016) to generate a range of pin fin geometries and meshes that are deployed as a large array of parallel CFD simulations in the Center for High Throughput Computing. The Engineering Equation Solver (EES) software (Klein, 2015) is used to develop correlations, which can then be implemented into heat exchanger optimization models. The predicted performance is compared to experimental data. The as-printed vs as-designed heat transfer surfaces are compared.

1. INTRODUCTION

In a world with a decreasing supply of fresh water, the power production industry is looking for design solutions that depend less on the availability of water. Dry-cooled condensers are one possibility, but they must compete with traditional water-cooled condensers in terms of cost, performance, and fan power. To improve performance, air-side heat transfer designs must be improved. Additive manufacturing offers the freedom to create designs that are difficult to manufacture with traditional methods. While the materials for additive manufacturing are not as conductive as the metals used in conventional heat exchangers, highly filled polymers do allow an order of magnitude improvement in conductivity and strength over the traditional materials used in 3D printing. In addition, control over the printing material offers other advantages such as the use of an antimicrobial infused filament.

The ultimate goal of this research is to design an air-side geometry capable of achieving the same thermal and hydrodynamic performance (heat transfer rate and pressure drop under a given set of operating conditions) as a conventional heat exchanger but at lower cost (i.e., using less material and/or less expensive manufacturing techniques). Because additive manufacturing allows for freedom in design, unconventional air-side geometries have been investigated using Computational Fluid Dynamics (CFD).

This work specifically investigates axially-tapered pin fin array geometries because of their ability to improve the air-side performance of heat exchangers. The typical evaluation process for any candidate geometry includes an initial CFD simulation to validate the results and determine mesh convergence followed by an extensive parametric study to

generate a data set sufficient to develop correlations in terms of dimensionless parameters. The correlations can then be implemented into a comprehensive heat exchanger model to allow for a thorough optimization and comparison between various geometries.

2. GEOMETRY DEFINTITION

The geometry of a bank of axially tapered fins is defined by the transverse and longitudinal pitches (S_T and S_L) with the pin shape itself defined by base and minimum diameters (D and D_{min}) and height (h). These dimensions are labeled for the bank of tapered pins in **Error! Reference source not found.** with fluid entering the first row of pins from the left and exiting to the right. In this work, only banks with uniform pin shapes are investigated.

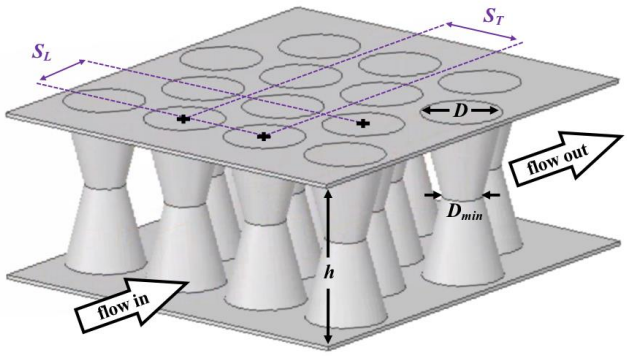

Figure 1: A tapered pin fin array

S_T is the center-to-center distance between two neighboring pins in any given row and S_L is the longitudinal center-to-center distance. The pins have a staggered geometric layout, meaning that the even rows (e.g., the second and fourth, etc.) are offset from the odd rows (the first and third, etc.) by a distance of $S_T/2$.

The dimensional pitches (i.e., S_T and S_L) are normalized by the base diameter D to define the dimensionless transverse pitch $\overline{S_T}$ and dimensionless longitudinal pitch $\overline{S_L}$:

$$\overline{S_T} = \frac{S_T}{D} \tag{1}$$

$$\overline{S_L} = \frac{S_L}{D} \tag{2}$$

This work investigates values of $\overline{S_T}$ that lie between 1.25 and 2.5 and values of $\overline{S_L}$ that lie between 0.625 and 2.0. If either dimensionless pitch falls below those ranges (e.g., $\overline{S_T}$ < 1.25 or $\overline{S_L}$ < 0.625), then the pressure drop across the bank was found to be too large to be practically useful. If either dimensionless pitch exceeds those ranges ($\overline{S_T}$ > 2.5 or $\overline{S_L}$ > 2.0), then the flow across the bank approaches the behavior of flow past a single pin. The optimal combination of dimensionless pitches was found to lie within the simulated range during heat exchanger optimization.

The shape of a fin is defined by two dimensionless parameters: the degree of taper T and the dimensionless height H. These parameters are defined as follow:

$$T = 1 - \frac{D_{\min}}{D} \tag{3}$$

$$H = \frac{h}{D} \tag{4}$$

Pins with various degrees of taper are shown in Figure 2. When $T = 0$, the pin has a straight-cylinder (i.e., tube) shape. As T increases, the minimum diameter of the pin decreases and the pin takes on an hourglass shape. Finally, when $T = 1$, D_{min} approaches 0 and the pin has a maximum taper. Degrees of taper T spanning from 0 to 1 are investigated in this work. This work investigates dimensionless heights H between 0.5 and 6.

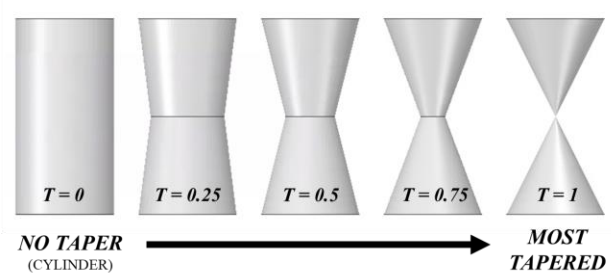

Figure 2: Pins with various degrees of taper

3. MODEL OF TAPERED PIN FIN ARRAYS

3.1 Geometry Generation

Each geometry was generated using ANSYS DesignModeler (ANSYS, 2016). Every geometry included inlet and outlet air blocks, in addition to the computational domain, so that simulation data is not impacted by entrance or exit effects. The inlet and outlet air blocks and computational domain of a bank of tapered pins geometry are shown in **Figure 1**. The base diameter D, the minimum diameter D_{min}, the height h, the longitudinal pitch S_L, and transverse pitch S_T are also shown in **Figure 1**.

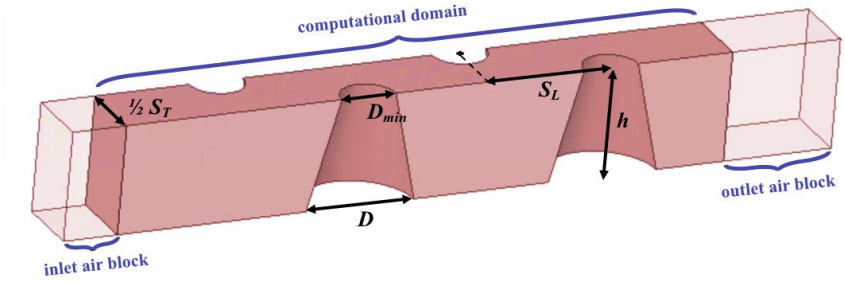

Figure 1: The inlet and outlet air blocks (transparent) and computational domain (shown as solid) of a pin fin array

By parametrically varying D_{min}, h, S_L, and S_T within ANSYS DesignModeler, each geometry could be modeled. The combination of S_L and S_T determined the geometric layout whereas D_{min} and h determined the pin shape. This work generated geometries with the parameter values listed in **Table 1**. For all geometries, D = 2 mm.

Table 1: Values for Geometric Parameters

		Transverse pitch S_T [mm]					
		1.25	**1.5**	**1.75**	**2**	**2.25**	**2.5**
Longitudinal pitch S_L [mm]	**0.625**			x	x	x	x
	0.75		x	x	x	x	x
	0.875	x	x	x	x	x	x
	1.125	x	x	x	x	x	x
	1.5	x	x	x	x	x	x
	2	x	x	x	x	x	x

Degree of taper T	**0**	**0.25**	**0.5**	**0.75**	**1**
D_{min} [mm]	2	1.5	1	0.5	0

Dimensionless height H	**0.5**	**1.25**	**2**	**4**	**6**
h [mm]	1	2.5	4	8	12

All combinations of S_L and S_T specified in Table 1 were modeled, which amounted to 33 unique geometric layouts. For each unique geometric layout, every combination of D_{min} and h were modeled. Therefore, a total of 825 unique geometries were modeled.

3.2 Modeling Criteria and Equations

The inlet velocity u_{inf} was varied to simulate Reynolds numbers (Re) between 30 and 1000. This range has been found to be near optimal for the heat exchangers considered in this work. In this work, Re was defined by:

$$\mathrm{Re} = \frac{u_{\mathrm{inf}} D}{\nu} \tag{5}$$

where D is the base diameter of the pin and ν is the kinematic velocity of the fluid ($\nu = \mu / \rho$).

All simulations in this work were modeled as being steady state. ANSYS Fluent solved a coupled set of conservation equations for each simulation including the continuity, momentum, and energy equations. These equations balanced mass, momentum, and energy.

For all simulations in this work, the fluid cell zone was set to air and Fluent's default properties for air were used: a density ρ = 1.225 kg/m^3, a heat capacity c_p = 1006.4 J/kg-K, a conductivity k = 0.0242 W/m-K, and a viscosity μ = 1.789 x 10^{-5} kg/m-s. These constant values were used in all calculations too.

To simulate case 1 (heated pins – with the objective of obtaining the heat transfer coefficient between the pin surface and the fluid), the pins were modeled as walls with uniform surface temperature T_s = 400 K and the bottom of the computational domain was modeled as an adiabatic wall. To simulate case 2 (heated bases – with the objective of obtaining the heat transfer coefficient between the base surface and the fluid), the pins were modeled as adiabatic walls and the bottom of the computational domain was modeled as a wall with uniform surface temperature T_s = 400 K. The boundary condition assignments are labeled in Figure 4.

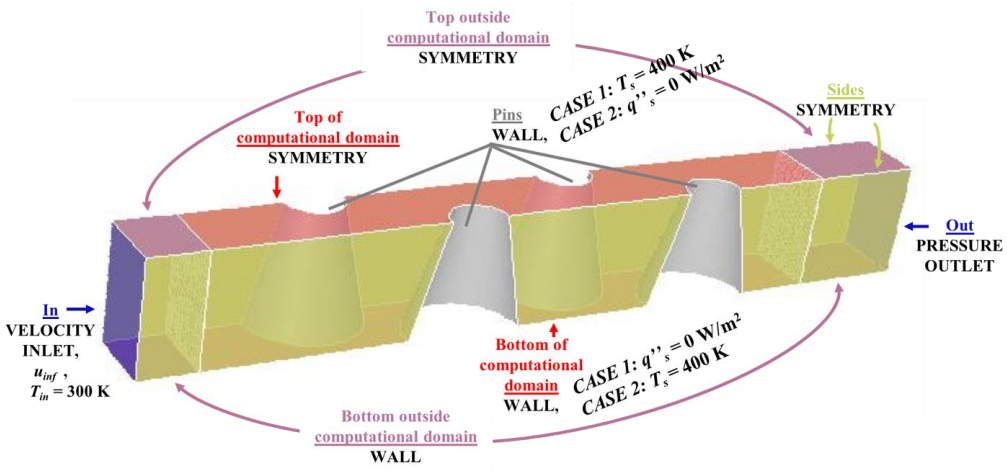

Figure 4: Boundary zone assignments for a bank of tapered pins

For both cases, air entered at plane In with a uniform velocity u_{inf} and temperature T_{in} = 300 K then traversed through the inlet air block, the Start interface, the Computational Domain, the End interface, and finally exited at plane Out, which was modeled as a pressure-outlet with a gauge pressure of 0 Pa.

4. PREDICTED PERFORMANCE FROM SIMULATIONS

4.1 Calculation of Performance Parameters

After running simulations, the data were extracted from three output text files, which reported the pin surface area, the pressure of the fluid at the Start and End mesh interfaces, and the mean temperature of the fluid at the Start and End mesh interfaces. These data were used to calculate dimensional performance metrics including the pressure drop, Δp, between the computational domain's inlet and outlet and the heat transfer coefficient $\overline{h}$. Then these dimensional performance metrics were used to find the dimensionless quantities: friction factor *f* and average Nusselt number $\overline{Nu}$.

The friction factor *f* is related to the pressure drop across a row of pins and the average Nusselt number $\overline{Nu}$ is related to the average heat transfer coefficient. Both dimensionless parameters can be correlated against Reynolds numbers Re (note that the Prandtl number used for the simulations is consistent with air, 0.7, and was not varied during this work as the only fluid of interest is air).

The pressure drop across the bank Δp was found each time the inlet velocity was updated (i.e., for the full range of Reynolds number) by subtracting the average outlet pressure p_{in} from the average inlet pressure p_{out}:

$$\Delta p = p_{in} - p_{out} \tag{6}$$

Values for p_{in} and p_{out} were extracted from the simulation by taking the area-weighted average pressure at the Start and End mesh interfaces, respectively.

The pressure drop, Δp, can be used to calculate the friction factor *f* as follows:

$$f = 2\frac{\Delta p}{\rho u_{\inf}^{\ 2} N_L} \tag{7}$$

where N_L is the number of rows (N_L = 4 in this work) and u_{inf} is the inlet velocity.

The average heat transfer coefficient $\overline{h}$ was also found for each value of *Re* using the ε- *NTU* method. The effectiveness ε of the bank is defined by:

$$\varepsilon = \frac{T_{out} - T_{in}}{T_s - T_{in}} \tag{8}$$

where T_s is the specified temperature of the heated surface and T_{in} and T_{out} are the mass-weighted average (or bulk) temperatures of the fluid at the inlet and outlet, respectively. The values for T_s and T_{in} are held constant in simulations (T_s = 400 K and T_{in} = 300 K). The value for T_{out} is extracted by taking the mass-weighted average temperature at the computational outlet. The effectiveness was used to find the number of transfer units, or *NTU*. For heat exchangers with one fluid and a constant wall temperature, *NTU* is calculated as follows (Nellis and Klein, 2009):

$$NTU = -\ln(1-\varepsilon) \tag{9}$$

The result for *NTU* is then used to find the average heat transfer coefficient $\overline{h}$:

$$\overline{h} = \frac{NTU\ \dot{m}\ c_p}{A_s} \tag{10}$$

where A_s is the area of the heated surface (the pins for case 1 and the base for case 2) and $\dot{m}$ is the mass flow rate of the fluid. The average Nusselt number $\overline{Nu}$ can be found using:

$$\overline{Nu} = \frac{\overline{h}\ D}{k} \tag{11}$$

where *D* is the base diameter. After obtaining a set of $\overline{Nu}$ values for a given bank, they can be correlated against the corresponding set of Re. Equation (15) was evaluated to find both $\overline{Nu}_{pins}$ and $\overline{Nu}_{base}$.

4.2 Correlation Development

Each dimensionless performance parameter (i.e., *f* and $\overline{Nu}$) was correlated with *Re*, $\overline{S_L}$, $\overline{S_T}$, *H*, and *T*.

$$f = f\left(\mathrm{Re}, S_L, S_T, H, T\right) \tag{12}$$

$$\overline{Nu} = f\left(\mathrm{Re}, S_L, S_T, H, T\right) \tag{13}$$

The regression equation for all three performance parameters was a 2nd order polynomial with cross terms. These functional relations are defined as follows:

$$\begin{aligned}\ln(f) = {} & \ln(a_0) + a_1 \ln(H) + a_2 \ln\left(H\right)^2 + a_3 \ln\left(\overline{S_L}\right) + a_4 \ln\left(\overline{S_L}\right)^2 + a_5 \ln\left(\overline{S_T}\right) + a_6 \ln\left(\overline{S_T}\right)^2 + \\ & a_7 \ln(\mathrm{Re}) + a_8 \ln(\mathrm{Re})^2 + a_9 T + a_{10} T^2 + a_{11} \ln\left(L_c\right) + a_{12} \ln\left(L_c\right)^2 + a_{13} \ln\left(H\right) \ln\left(\overline{S_L}\right) + \\ & a_{14} \ln\left(H\right) \ln\left(\overline{S_T}\right) + a_{15} \ln\left(H\right) \ln\left(\mathrm{Re}\right) + a_{16} \ln\left(H\right) T + a_{17} \ln\left(H\right) \ln\left(L_c\right) + a_{18} \ln\left(\overline{S_L}\right) \ln\left(\overline{S_T}\right) + \\ & a_{19} \ln\left(\overline{S_L}\right) \ln\left(\mathrm{Re}\right) + a_{20} \ln\left(\overline{S_L}\right) T + a_{21} \ln\left(\overline{S_L}\right) \ln\left(L_c\right) + a_{22} \ln\left(\overline{S_T}\right) \ln\left(\mathrm{Re}\right) + a_{23} \ln\left(\overline{S_T}\right) T + \\ & a_{24} \ln\left(\overline{S_T}\right) \ln\left(L_c\right) + a_{25} \ln\left(\mathrm{Re}\right) T + a_{26} \ln\left(\mathrm{Re}\right) \ln\left(L_c\right) + a_{27} T \ln\left(L_c\right)\end{aligned} \tag{14}$$

$$\begin{aligned}\ln(\overline{Nu}) = {} & \ln(b_0) + b_1 \ln(H) + b_2 \ln\left(H\right)^2 + b_3 \ln\left(\overline{S_L}\right) + b_4 \ln\left(\overline{S_L}\right)^2 + b_5 \ln\left(\overline{S_T}\right) + b_6 \ln\left(\overline{S_T}\right)^2 + \\ & b_7 \ln(\mathrm{Re}) + b_8 \ln(\mathrm{Re})^2 + b_9 T + b_{10} T^2 + b_{11} \ln\left(L_c\right) + b_{12} \ln\left(L_c\right)^2 + b_{13} \ln\left(H\right) \ln\left(\overline{S_L}\right) + \\ & b_{14} \ln\left(H\right) \ln\left(\overline{S_T}\right) + b_{15} \ln\left(H\right) \ln\left(\mathrm{Re}\right) + b_{16} \ln\left(H\right) T + b_{17} \ln\left(H\right) \ln\left(L_c\right) + b_{18} \ln\left(\overline{S_L}\right) \ln\left(\overline{S_T}\right) + \\ & b_{19} \ln\left(\overline{S_L}\right) \ln\left(\mathrm{Re}\right) + b_{20} \ln\left(\overline{S_L}\right) T + b_{21} \ln\left(\overline{S_L}\right) \ln\left(L_c\right) + b_{22} \ln\left(\overline{S_T}\right) \ln\left(\mathrm{Re}\right) + b_{23} \ln\left(\overline{S_T}\right) T + \\ & b_{24} \ln\left(\overline{S_T}\right) \ln\left(L_c\right) + b_{25} \ln\left(\mathrm{Re}\right) T + b_{26} \ln\left(\mathrm{Re}\right) \ln\left(L_c\right) + b_{27} T \ln\left(L_c\right)\end{aligned} \tag{15}$$

where $a_0, \ldots, a_{27}$ and $b_0, \ldots, b_{27}$ are regression constants, and L_c is the dimensionless clearance between diagonal pins, which is defined as follows:

$$L_c = \sqrt{\frac{1}{4}\overline{S_T}^2 + \overline{S_L}^2} - 1 \tag{16}$$

The dimensionless parameter L_c quantified how closely or loosely packed a bank was.

The closeness of fit of each correlation was assessed by comparing correlation predictions with corresponding simulation data. Correlation predictions were obtained by evaluating the correlations with every combination of input parameters that was simulated. Figures 5, 6, and 7 shows correlation predictions plotted against corresponding simulation data for $\overline{Nu}_{pins}$, $\overline{Nu}_{base}$, and f, respectively. Each plot includes data points for all 8,250 simulations, a line of perfect correlation (solid blue line) and lines indicating correlation variances of +10%, -10%, +20%, and -20% from simulation data (red dashed lines).

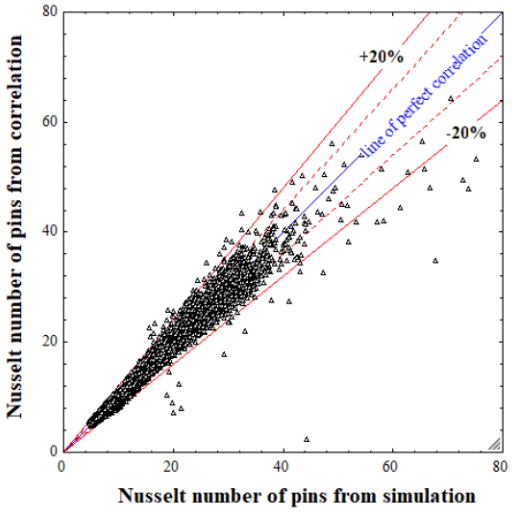

Figure 5: Correlation vs simulation pin Nusselt number of pins

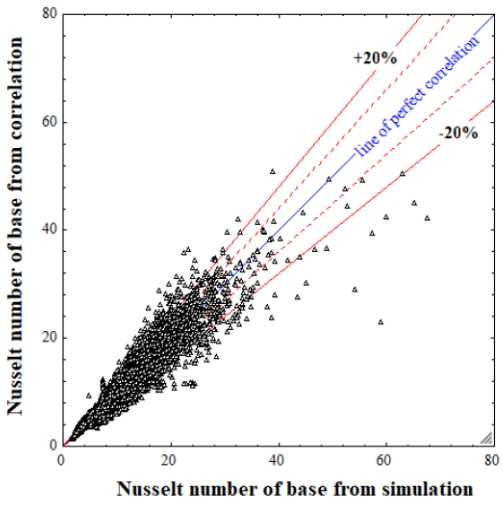

Figure 6: Correlation vs simulation Nusselt number of base

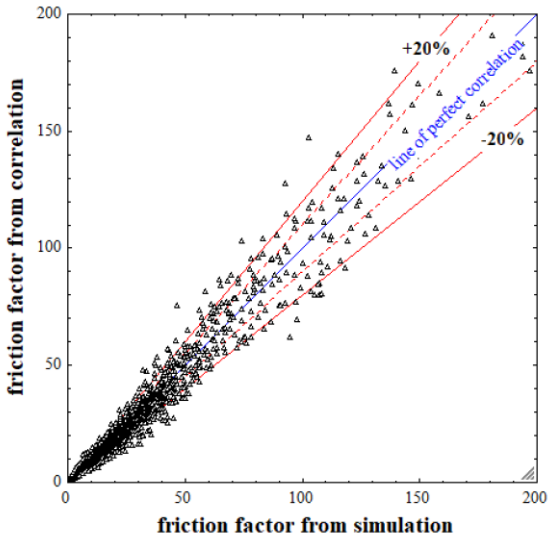

Figure 7: Correlation vs simulation friction factor

The set of correlations predicted simulation data as follows: 99.1% of $\overline{Nu}_{pins}$ correlation values were within 20% of simulation data, whereas 87.5% of $\overline{Nu}_{base}$ correlation values and 92.4% of f correlation values were within 20% of simulation data.

5. PERFORMANCE OF TAPERED PIN FINS

The correlations were implemented into an optimization model in order to investigate the influence of fin taper on heat exchanger performance. The model carried out a constrained optimization in order to determine the optimal heat exchanger configuration (e.g., pitch and fin diameter) that minimized mass for given set of operating conditions and a specified effectiveness and air-side pressure drop. The resulting normalized heat exchanger mass is plotted against the degree of taper in Figure 8 (the mass is normalized by the mass of a heat exchanger using cylindrical fins, $T = 0$).

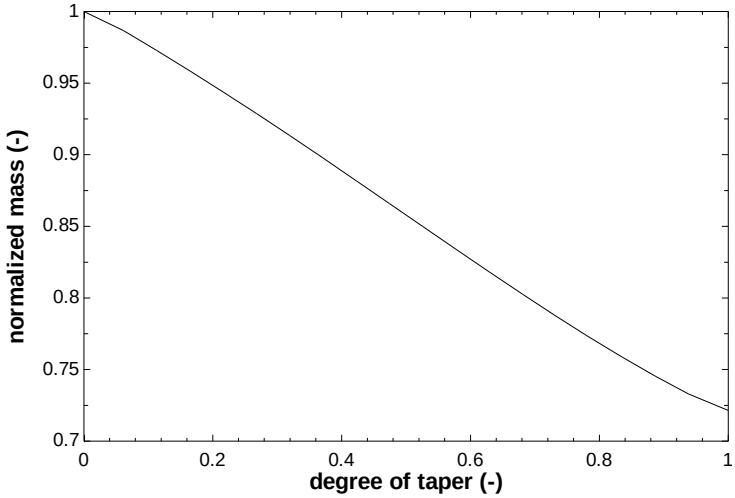

Figure 8: Normalized mass of heat exchanger vs degree of taper

As expected, less mass (i.e., material) is required with increasing fin taper in order to achieve the same effectiveness at the same pressure drop. As shown in Figure 11, the most tapered fin ($T = 1$) requires approximately 25 % less mass to achieve the same performance as a cylindrical fin ($T = 0$).

6. COMPARISON OF MODELED AND PRINTED GEOMETRY

6.1 Overview of Printed Tapered Pin Fins

The printed geometry varies from the modeled geometry. Print settings such as bed temperature, extrusion multipliers, print speed, feature size, and layer height can affect the quality of the print. Figure 9 is a 3D-rendering of CT scans taken from a single fin. Instead of a smooth, cone-like surface, the fins have ridges about 0.1 mm in height, corresponding to the specified layer height of the print. The resolution of this particular scan was 18 µm.

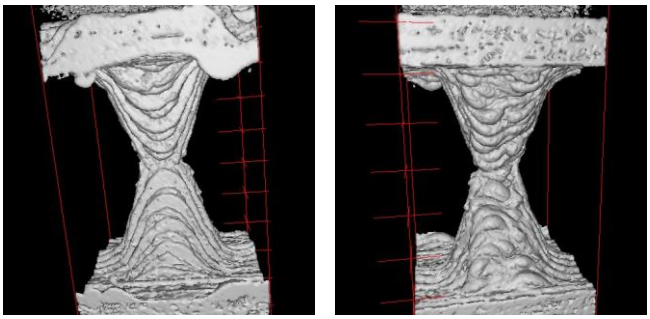

Figure 9: 3D-rendering of CT scans of a single tapered fin

One side of the fin is less organized and has sporadic clumps of material (left), while the opposite side has parabolic layers (right). The clumps of material are due to gravity pulling the material down as it prints because the first layer is printed with no support. One concern is variation in performance associated with slight variations in the prints. A program was written to analyze the scans and output statistics associated with the printed geometry.

In general, the cross-section of the printed fins is more rectangular than circular for fins printed at this scale. Figures 10 and 11 show a scan of the heat exchanger cross-section taken at the axial location of minimum and maximum diameters (D_{min} and D_{max}), respectively, that was analyzed. The direction of airflow is from the bottom of the page to the top of the page. If the fins printed as modeled, the cross-sectional area of the fins at D_{min} would be 0.196 mm^2 and the major and minor axes would be the same and equal to 0.5 mm, corresponding to the minimum diameter. Tables 2 and 3 provide the variation in size of the fins at D_{min} and D_{max}, respectively, for a single channel.

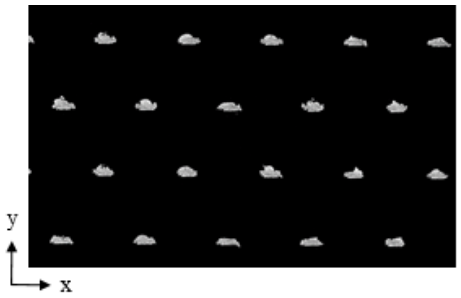

Figure 10: CT scan of fins at minimum diameter

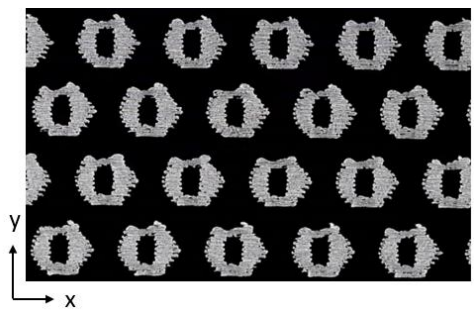

Figure 11: CT scan of fins at maximum diameter

Table 2: CT scan statistics and as-designed dimensions at minimum diameter

	As-designed	As-measured		Equivalent Diameter
	Avg.	Avg.	St. Dev.	
Major axis (mm)	0.500	0.975	0.07	0.610
Minor axis (mm)		0.480	0.67	
Area (mm^2)	0.196	0.297	0.03	0.196

Table 3: CT scan statistics and as-designed dimensions at maximum diameter

	As-designed	As-measured		Equivalent Diameter
	Avg.	Avg.	St. Dev.	
Major axis (mm)	2.500	2.736	0.03	2.380
Minor axis (mm)		2.304	0.04	
Area (mm^2)	4.909	4.399	0.07	4.909

The gross geometry of the fins along with the surface features do not coincide exactly with the model from which they were printed, or the simulation models used to generate the corresponding correlations.

6.2 Performance Comparison

The experimental airside performance of the printed heat exchanger was compared to the theoretical performance of the heat exchanger using the developed correlations. Figure 12 displays the data for one particular heat exchanger. The model curve is the predicted performance using the geometric parameters as modeled. The modified model curve is the predicted performance based on tapered pin fins with equivalent cross-sectional area to the averaged area measured using the CT scans.

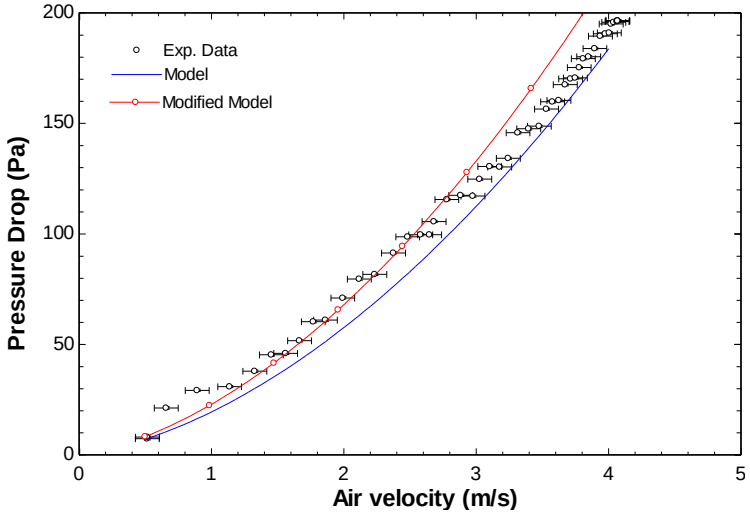

Figure 12: Performance of printed fins compared to modeled fins

While the surface of the printed fins differs from the model that was used to create the correlations, the model agrees well with the experimental data. Future work will be done to characterize at what point the surface roughness due to the print will have a significant effect on the performance. Because 3D-printed heat exchangers are a relatively new development, the effects of the printed surface on performance are currently being investigated. Although the gross size of the geometry was not as designed, the increase in surface area provided by the printed surface increased the heat transfer as seen in a previous study (Kirsch, 2017).

7. CONCLUSIONS

With continually advancing manufacturing techniques such as additive manufacturing, novel geometries can be implemented in heat exchangers. CFD allows for the creation of correlations to predict and optimize performance, as shown for the axially-tapered pin-fin arrays in this work. Due to various factors in the printing process, the heat exchangers do not print as-designed. By scanning the print and using image analysis, the printed geometry can be implemented into the correlations and accurately predict the performance of the heat exchanger. Future work will be done to characterize the effect of the increased surface roughness that 3D-printing creates.

NOMENCLATURE

A_s	surface area	(m^2)
c_p	heat capacity	(J/K)
D	base diameter	(m)
D_{min}	minimum diameter	(m)
h	pin-fin height	(m)
H	dimensionless height	(–)
$\overline{h}$	avg heat transfer coefficient	(W/ m^2-K)

f	friction factor	(–)
k	thermal conductivity	(W/m-K)
$\dot{m}$	mass flow rate	(kg/s)
N_L	number of rows	(–)
$\overline{Nu}$	avg Nusselt number	(–)
NTU	number of transfer units	(–)
p	pressure	(Pa)
Δp	pressure drop	(Pa)
Re	Reynolds number	(–)
S	pin-fin pitch	(–)
$\overline{S}$	dimensionless pin-fin pitch	(m)
T	temperature, degree of taper	(K), (–)
u_{inf}	inlet velocity of fluid	(m/s)

Greek

ε	effectiveness	(–)
μ	viscosity	(Pa-s)
ρ	density	(kg/m^3)
ν	kinematic viscosity	(m^2/s)

Subscript

base	base
in	inlet
L	longitudinal
out	outlet
pins	pin fins
T	transverse

REFERENCES

(2016). *ANSYS Academic Research Mechanical*, Release 17.1.

Kirsch, K. L., Thole, K. A. (2017). Pressure loss and heat transfer performance for additively and conventionally manufactured pin fin arrays. *International Journal of Heat and Mass Transfer*, 108, 2512.

Klein, S.A. (2015). *Engineering Equation Solver (EES)*, Version 10.063, F-Chart software.

Nellis, G.F. & Klein, S.A. (2009). *Heat Transfer*. New York, NY: Cambridge University Press.

Žukauskas, A. (1972). Heat transfer from tubes in crossflow. Advances in Heat Transfer, Vol. 8. J.P. Harnett & T.F. Invine, Jr. (Eds.). New York, NY: Academic Press.

ACKNOWLEDGEMENTS

The information, data, or work presented herein was funded in part by the Advanced Research Projects Agency-Energy (ARPA-E), U.S. Department of Energy, under Award Number DE-AR0000573. The views and opinions of authors expressed herein do not necessarily state or reflect those of the United States Government or any agency thereof. This work was also made possible through the support of Jake Boxleitner at UW-Madison.